

Impact of soil freezing–thawing processes on August rainfall over southern China

Kun Xia^{1,*}, Lijuan Li¹, Yanli Tang², Bin Wang¹

¹State Key Laboratory of Numerical Modeling for Atmospheric Sciences and Geophysical Fluid Dynamics, Institute of Atmospheric Physics, Chinese Academy of Sciences, Beijing, China

²State Key Laboratory of Severe Weather, Chinese Academy of Meteorological Sciences, Beijing, China

Corresponding author: Kun Xia (xiakun@lasg.iap.ac.cn)

Key Points:

- The model with considering supercooled water in freezing-thawing schemes reproduces the climatology and trend of the August rainfall in Southern China.
- The majority of the increasing August rainfall in Southern China is balanced by the dynamic processes of the vertical moisture advection, relating to changes in atmospheric circulation
- It provides a new interpretation for the ‘southern flooding’ during 1979–2008 from the point of frozen soil changing

Abstract

In this study, the impact of soil freezing–thawing processes on August rainfall in southern China (SC) during 1979–2008 and related physical mechanisms are investigated using the Grid-Point Atmospheric Model version 2.0 (GAMIL2.0). This model with considering the supercooled water in soil freezing–thawing scheme reproduces the climatology and trends of August precipitation in the SC region. Moisture-budget analysis is employed to quantify the contributions of different factors to the change of precipitation in SC. The results indicate that evaporation contributes significantly to the climatologically August rainfall in SC. The dynamic component of vertical moisture advection, which is related to changes in atmospheric circulation, plays an important role in August precipitation trends. The possible physical mechanism is that the GAMIL2.0 considering the supercooled water simulated much higher soil/air temperature on August especially in the north of 40°N, weakened the meridional thermal contrast, decreased the 200hpa zonal winds, strengthened 850hpa northerly wind, which is more beneficial to the convergence in SC and lead to the precipitation increased. This study provides a new interpretation of the ‘southern flooding’ during 1979–2008 from the point of frozen soil changing.

1 Introduction

Southern China (SC), including regions south of the Yangtze River and east of the Tibetan Plateau (TP), is greatly affected by droughts and floods due to the long flood season and large interannual and interdecadal variations in rainfall. During 1951–2010, most extreme precipitation events occurred south of 34°N, and resulted in huge economic losses (Chen & Zhai, 2013). In addition, the number of records of flood disaster has an increasing trend at a rate of 77.4 times per decade from 1984 to 2010 (Shi et al., 2020). Improved our understanding of summer rainfall in SC should not

only enhance our ability to predict rainfall in flood seasons, but also increase capacity for preventing floods, controlling drought, and mitigating natural disasters.

Precipitation in SC occurs from April to September or early October. The April–June period is the ‘pre-rainy’ season and July–September the ‘second flood’ season. Monthly rainfall is variable during May–August, but the total for this period exceeds half the total annual rainfall (Su et al., 2014). Previous studies have suggested dividing the summer rainy season into early and late periods or treating each month separately when investigating variations in precipitation in SC (Wang et al., 2009; Yuan et al., 2019). August has the highest (and variable) precipitation during the second flood season, but most previous studies have focused on early summer rainfall (Chan et al., 2005; Li et al., 2017). This study therefore focuses mainly on August rainfall in SC.

The summer rainfall in SC has undergone a significant interdecadal increase since the mid-1990s, with a ‘dipole’ pattern—the so-called ‘southern flood and northern drought’ since the late 1970s, by using the reanalysis and observational precipitation data of the China Meteorological Administration (Ding et al., 2008; Kwon et al., 2007; Wu et al., 2010; Yao et al., 2008; Zhang et al., 2008; Zhu et al., 2011).

External forcing factors have contributed to the interdecadal variation and long-term trend. Previous studies have highlighted the role of sea surface temperature (SST) anomalies in different key regions (Wu et al., 2010; Liu et al., 2019), including the Atlantic Multidecadal Oscillation and the Pacific Decadal Oscillation (Zhu et al., 2015; Si & Ding, 2016; Wu & Mao, 2017; Yuan et al., 2019). In addition, tropical cyclones have contributed appreciably to precipitation in SC (Ren et al., 2006; Su et al., 2014). The increasing incidence of typhoons has been largely responsible for the

increased precipitation in southeastern China since the mid-1990s (Kwon et al., 2008). Recently, the impact on rainfall of external forcing by human activity is attracting attention, including land-use changes and anthropogenic aerosol emissions (Li et al., 2019). Modeling studies have shown that anthropogenic aerosols such as black carbon may contribute to the increased incidence of summer floods in SC (Menon et al., 2002; Jiang et al., 2017), while large-scale urbanization over eastern China may lead to weakened precipitation over southern East Asia in the late summer (Ma et al., 2015; Chen et al., 2016).

Other studies have shown that variations of snow cover in spring and winter over the TP and Eurasia play an important role in the East Asia precipitation during the following summer (Wu et al., 2009; Zhang et al., 2013). Preceding winter and spring snow anomalies over the TP affect summer precipitation in eastern China, with correlation between winter snow cover and subsequent summer rainfall being negative in areas of southern and far-northern China, and positive in the middle–lower reaches of the Yangtze River. Spring snow cover anomalies in the TP are therefore considered important predictors of summer rainfall in China (Chen & Wu, 2000; Wu et al., 2010; Zhang et al., 2008; Zhang et al., 2017).

Apart from snow cover, frozen soil is distributed widely over mid–high latitudes in the Northern Hemisphere. Transitions between freezing and thawing processes may cause changes in diabatic surface heating. Some studies have reported that the inclusion of soil freeze–thaw processes in land-surface and climate models simulate realistic soil temperatures, soil water contents, surface energy/moisutire fluxes, and runoff during the spring melt season (Cox et al., 1999; Koren et al., 1999; Viterbo et al., 1999; Schlosser et al., 2000; Niu & Yang, 2006). Others have indicated that the Eurasian regional climate is sensitive to frozen soil variability by comparing

simulations whether include the soil freezing parameterizations or with different complexity soil freezing-thawing schemes in land surface model (Poutou et al., 2004; Takata & Kimoto, 2000; Xin et al., 2012). Until now, however, there has been little study of the specific effects of frozen-soil changes on August rainfall in SC. Seasonal frozen soil at mid-high latitudes in the Northern Hemisphere has shown a clearly decreasing trend over recent decades, as indicated by using different data, such as observational soil freeze depth, freezing/thawing index and so on (Frauenfeld et al., 2007; Frauenfeld & Zhang, 2011; Peng et al., 2017; Xia & Wang, 2020). This study aimed to investigate whether changes in frozen soil affect August rainfall in SC, and further investigate how the frozen soil variability affects the August rainfall over SC, and what the mechanisms behind it. The remainder of this paper is organized as follows. Section 2 describes the model and related experiments, validated data, and methods used in this study. Section 3 presents the main results. Conclusions are given in Section 4.

2 Data and Methods

2.1 Model and experimental design

The Grid-Point Atmospheric Model version 2.0 (GAMIL2.0), developed by the State Key Laboratory for Numerical Modeling of Atmospheric Sciences and Geophysical Fluid Dynamics (LASG), Institute of Atmospheric Physics (IAP), Chinese Academy of Sciences (CAS), was applied with a horizontal resolution of about $2.8^{\circ} \times 2.8^{\circ}$, with high-latitude and polar regions having a weighted equal-area grid and other regions a Gaussian grid, and with 26- σ levels of vertical resolution with the topmost level at 2.194 hPa. The dynamic core of the model is based on a finite-difference scheme developed by Wang et al. (2004) and Wang & Ji (2006). Physical processes included

in the older version (GAMIL1.0) were mainly from the CAM2.0 model (Collins et al., 2003), but GAMIL2.0 includes improvements related to deep convection, cumulus clouds, and cloud microphysical schemes, among others (Li et al., 2013). GAMIL2.0 takes part in the Atmospheric Model Intercomparison Project (AMIP II) and CMIP5 as the atmospheric component of the Flexible Global Ocean–Atmosphere–Land System Model, Grid-Point version 2 (FGOALS-g2).

GAMIL2.0 is coupled with the Community Land Model version 3.0 (CLM3.0) (Oleson et al., 2004) developed by NCAR and is used as the land component in most CMIP5 climate system models. In CLM3.0, the critical temperature of soil freezing/thawing is 0°C; soil ice begins to melt at soil temperatures above 0°C and liquid water freezes at soil temperatures below 0°C in each soil layer. However, in fact, when the soil temperature is below the freezing point, ice and liquid water could coexist in the soil layer where excess liquid water freezes only when the liquid water content is above the maximum water content of the soil layer, as derived from the freezing-point-depression equation (Niu & Yang, 2006). Therefore, the concept of supercooled soil water (i.e., liquid water coexisting with ice over a wide range of temperatures below the freezing point) is introduced in phase-change processes in subsequent versions of CLM (e.g. CLM 4.0) Conditions under which a phase change occurs in CLM3.0 is considered the ‘A’ scheme, and considering supercooled soil water is the ‘B’ scheme, as described in Table 1.

Table 1. The two criteria for soil freezing and thawing.

Scheme	Thawing conditions	Freezing conditions
A	$T > T_{\text{frz}}$ and $\theta_{\text{ice}} > 0$	$T < T_{\text{frz}}$ and $\theta_{\text{liq}} > 0$

B	$T > T_{\text{frz}}$ and $\theta_{\text{ice}} > 0$	$T < T_{\text{frz}}$ and $\theta_{\text{liq}} > \theta_{\text{liq,max}}$
---	--	--

θ_{liq} and θ_{ice} are the soil liquid-water and ice content, respectively; T_{frz} is the freezing temperature

of water (273.16 K); $\theta_{\text{liq,max}}$ is the maximum liquid-water content at $T < T_{\text{frz}}$.

The maximum soil liquid-water content, $\theta_{\text{liq,max}}$, is calculated using equation (1):

$$\theta_{\text{liq,max}} = \theta_{\text{sat}} \left\{ \frac{10^3 L_f (T - T_{\text{frz}})}{g T \psi_{\text{sat}}} \right\}^{-1/b} \quad (1)$$

where L_f is the latent heat of fusion (J kg^{-1}); g is gravitational acceleration (m s^{-2});

ψ_{sat} and b are the soil-texture-dependent saturated matric potential (mm) and Clapp

and Hornberger (1978) exponent, respectively; T is temperature (K); and T_{frz} is the

freezing temperature of water (273.16 K).

To exclude the effect of sea temperature, we adopted climatological SST data as the

sea boundary. Two simulations were performed with GAMIL2.0 using the different

freezing/melting schemes (Table 1) during 1974–2008, with the control experiment

(CTRL) using the A scheme and the other (NEW) the B scheme. The first five years

were a spin-up, with the 30 yrs (1979–2008) being analyzed. The CMAP (Xie &

Arkin, 1997) and GPCP datasets (Adler et al., 2003), which were provided by the

NOAA/OAR/ESRL Physical Sciences Laboratory (PSL)

(<https://psl.noaa.gov/data/gridded/index.html>), were used to validate the simulations.

2.2 Methods

Moisture-budget analysis is widely used to separate dynamic and thermal

contributions to precipitation variability (Seager et al., 2010; Chou & Lan, 2012; Li et

al., 2018; Akinsanola & Zhou, 2019).

The moisture-budget equation is as follows:

$$P = -\left\langle \frac{\partial q}{\partial t} \right\rangle - \left\langle \nabla_h \cdot q \vec{V}_h \right\rangle - \left\langle \frac{\partial q \omega}{\partial p} \right\rangle + E + \delta \quad (2)$$

where P, E, and q represent precipitation, evaporation, and specific humidity, respectively; and δ is the residual term reflecting the influence of all nonlinear terms. The second and third term on the right of equation (2) represent the horizontal and vertical convergences of moisture flux, and ' $\langle \rangle$ ' represents the vertical mass integration from surface to tropopause (100hPa), which can be expressed as: $\langle Variable \rangle = \frac{1}{g} \int_{P_s}^{100} (Variable) dP$. The tendency

term, $-\left\langle \frac{\partial q}{\partial t} \right\rangle$, is small and can be neglected, with equation (2) being rewritten as:

$$P = -\left\langle \vec{V}_h \cdot \nabla_h q \right\rangle - \left\langle \frac{\omega \partial q}{\partial p} \right\rangle + E + \delta \quad (3)$$

and with changes in the precipitation being expressed as:

$$P' = -\left\langle \vec{V}_h \cdot \nabla_h q \right\rangle' - \left\langle \frac{\omega \partial q}{\partial p} \right\rangle' + E' + \delta' \quad (4)$$

where ' $\langle \rangle$ ' indicates the linear trend from 1979 to 2008 over area to be studied. The first and second terms on the right of equation (4) represent horizontal and vertical moisture advection, respectively. The $-\left\langle \frac{\omega \partial q}{\partial p} \right\rangle'$ term may be separated into three terms, as follows:

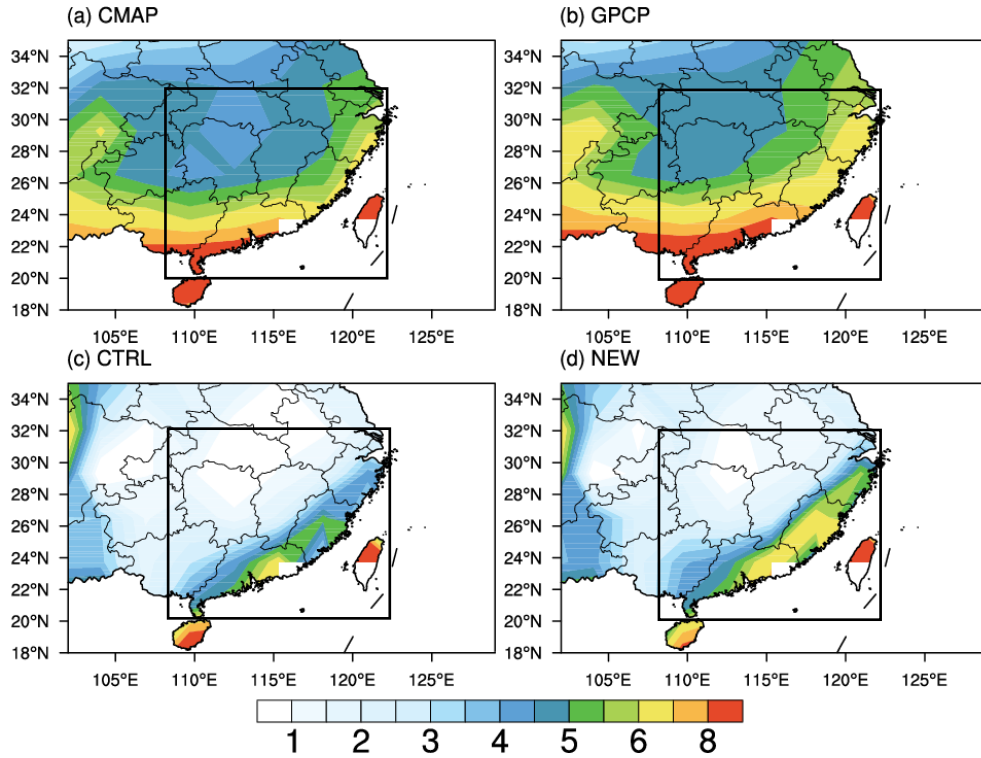
$$-\left\langle \frac{\omega \partial q}{\partial p} \right\rangle' = -\left\langle \frac{\omega' \partial \bar{q}}{\partial p} \right\rangle - \left\langle \frac{\bar{\omega} \partial q'}{\partial p} \right\rangle - \left\langle \frac{\omega' \partial q'}{\partial p} \right\rangle \quad (5)$$

where ' $\langle \bar{\ } \rangle$ ' indicates the climatology during 1979–2008. The first and second terms on the right of equation (5) are usually considered the dynamic and thermal components of vertical moisture advection, respectively. The dynamic component is associated with atmospheric

180 circulation changes while specific humidity is unchanged; the thermal component reflects the
 181 influence of specific humidity changes on precipitation. The third term on the right of
 182 equation (5) is a nonlinear term and is much smaller than the dynamic/thermal components,
 183 so is neglected here. To simplify the equations, ‘vdq’ and ‘wdq’ represent $\langle \vec{V}_h \cdot \nabla_h q \rangle$ and
 184 $\langle \frac{\omega \partial q}{\partial p} \rangle$, respectively, and $(vdq)'$ and $(wdq)'$ their trends; $(wdq)'$ and $(w'dq)$ denote the
 185 $\frac{\overline{\omega \partial q}}{\partial p}'$ and $\frac{\overline{\omega' \partial q}}{\partial p}$ terms, respectively.

186 3 Results

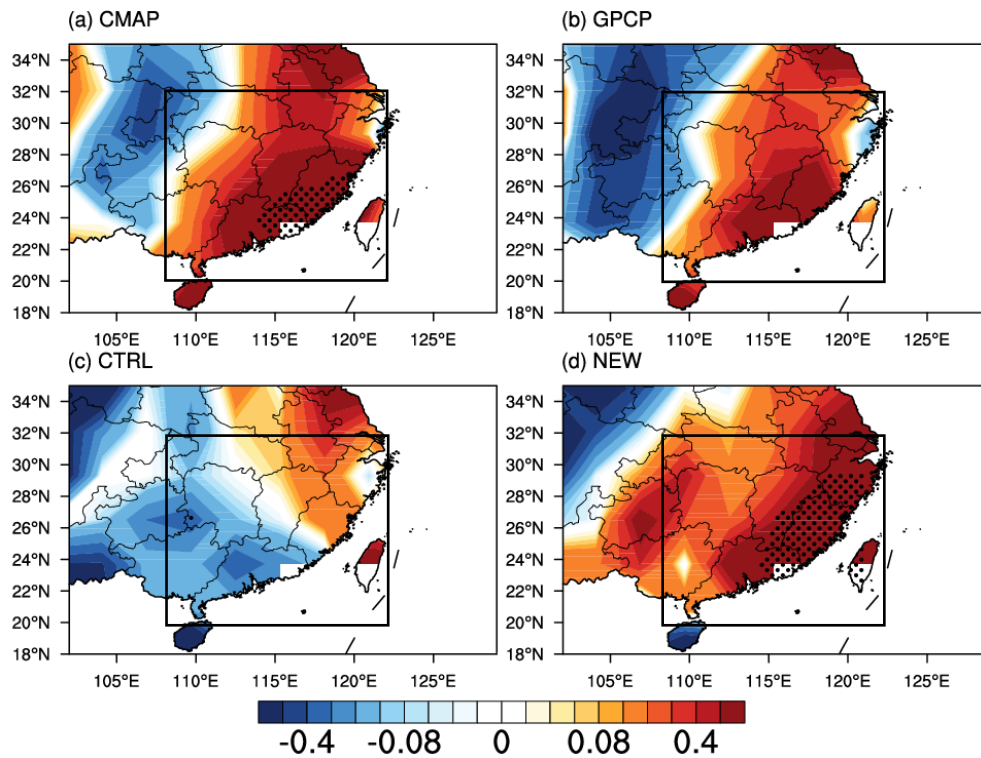
187 3.1 Evaluation of GAMIL2 simulations



188

189 **Figure 1.** Mean August precipitation (mm d⁻¹) in southern China during 1979–2008:
 190 observational data of (a) CMAP and (b) GPCP, and results of simulations (c) CTRL
 191 and (d) NEW. Rectangles represent the study area.

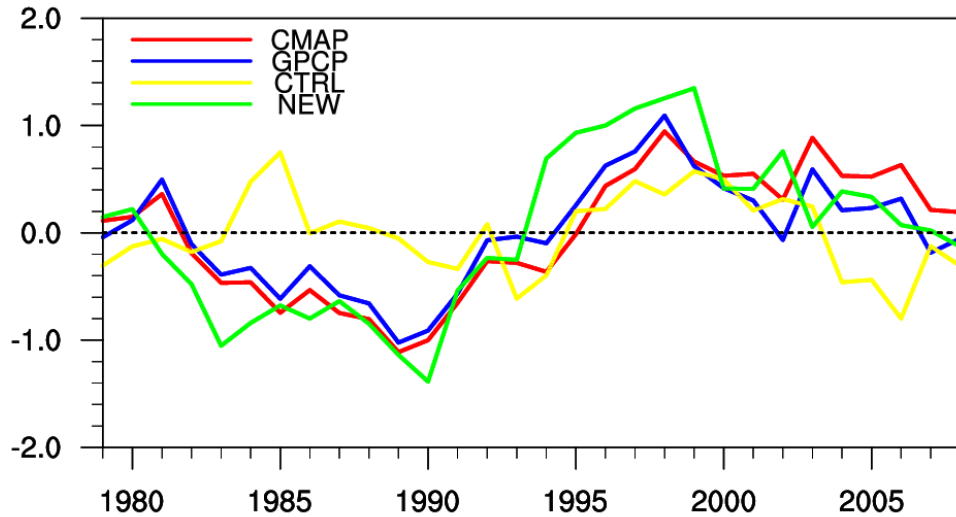
192 The mean August precipitation over SC during 1979–2008 is illustrated in Figure 1.
 193 The gridded CMAP and GPCP observations indicate that precipitation increases
 194 gradually from north to south, with the main precipitation center being located in
 195 southeastern China (Figure 1a, b). The CTRL simulation reasonably reproduces the
 196 spatial rainfall distribution with a pattern correlation coefficient (r) of 0.91 with
 197 CMAP and GPCP over the main precipitation region (20° – 32° N, 108° – 122° E)
 198 (Figure 1c), but underestimates the actual rainfall with a mean bias between CTRL
 199 and CMAP and GPCP of -2.55 mm d^{-1} and -3.04 mm d^{-1} , respectively. The NEW
 200 simulation has a lower mean CMAP and GPCP biases of -1.82 mm d^{-1} and -2.31 mm
 201 d^{-1} , respectively, although it has a dry bias in northern areas (Figure 1d).



203 **Figure 2.** Spatial distribution of long-term trends of August rainfall ($\text{mm d}^{-1}\text{decade}^{-1}$)
 204 over southern China, 1979–2008: observational data of (a) CMAP and (b) GPCP; and
 205 the (c) CTRL and (d) NEW simulations. Stippling indicates trends significant at the
 206 90% confidence level. The rectangle indicates the main study area.

207 The CMAP and GPCP data exhibit increasing long-term trends in August rainfall over
 208 the main precipitation region (Figure 2a, b). The CTRL simulation was almost

impossible to simulate the increasing trend (Figure 2c), but the NEW simulation captured this increasing trend well (Figure 2d).



211

Figure 3. Time series of August precipitation departures (mm d^{-1}) from climatological means (1979–2008) for the region 20° – 32°N , 108° – 122°E , based on CMAP (red), GPCP (blue), CTRL test (yellow) and NEW test (green) data. The lines represent nine-year running averages.

The ability of the CTRL and NEW simulations to reproduce area-average characteristics is demonstrated in the time series plots for August rainfall anomalies in the main precipitation region (Figure 3). Previous studies have shown interdecadal changes around 1992/93 for SC rainfall in the summer and in the individual months of June, July, and August (Ding et al., 2008; Wu et al., 2010; Su et al., 2014). The CMAP and GPCP observations exhibit obvious interdecadal rainfall variation around 1994, with pre-1994 summer rainfall being persistently lower than normal, and an abrupt post-1994 change to above normal (Figure 3). The observations are consistent, with correlation coefficients of up to 0.93, and are statistically significant at the 95% confidence level. The NEW simulation captures rainfall variations around 1993 well, with the highest correlation with CMAP ($r = 0.80$) and GPCP ($r = 0.85$). However, the CTRL simulation fails to describe the abrupt changing process around 1993/94,

showing only weak correlation with observations ($r = 0.11$ for CMAP and 0.21 for GPCP).

3.2 Moisture-budget analysis

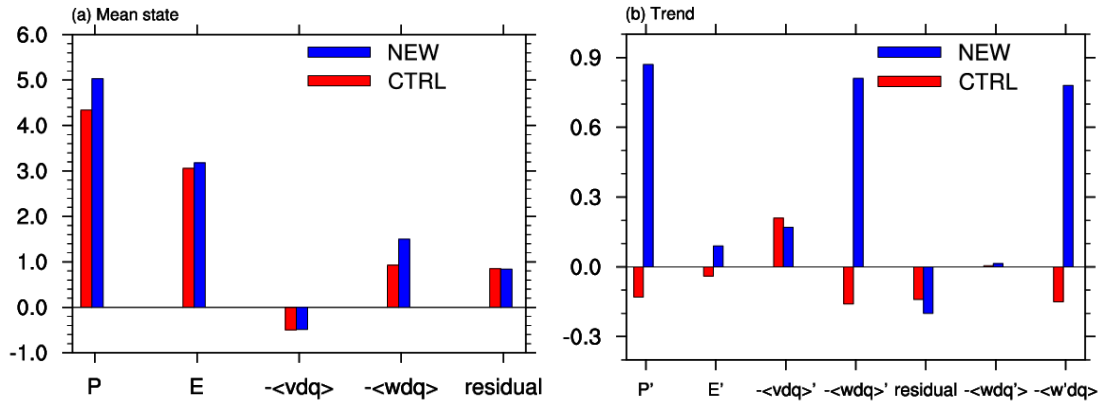


Figure 4. Regional area-averaged moisture-budget components in the main rainfall regions: (a) Mean state (mm d^{-1}) and (b) linear trend ($\text{mm d}^{-1} \text{decade}^{-1}$).

A moisture-budget analysis was undertaken for the main rainfall regions (20° – 32°N , 108° – 122°E) to elucidate why the NEW test simulated the August mean rainfall and long-term trends so well. Area-averaged moisture-budget components of precipitation in the main rainfall regions are shown in Figure 4. It is clear that the climatology of August rainfall is mainly contributed by local evaporation, indicating the importance of land–atmosphere interaction in the region. Vertical moisture advection is the second-ranked contributor, with horizontal moisture advection contributing little to the total precipitation (Figure 4a). The spatial distributions of evaporation and vertical moisture advection are shown in Figure 5. The patterns of evaporation simulated in the CTRL and NEW simulations (Figure 5a, b) are consistent with the rainfall pattern (Figure 1c, d), with rainfall increasing from northwest to southeast in SC. The difference in vertical moisture advection between the CTRL and NEW simulations (Figure 5c, d) is greatest in the north of GuangZhou provinces and south of FuJian provinces, respectively, consistent with their simulated mean August rainfalls.

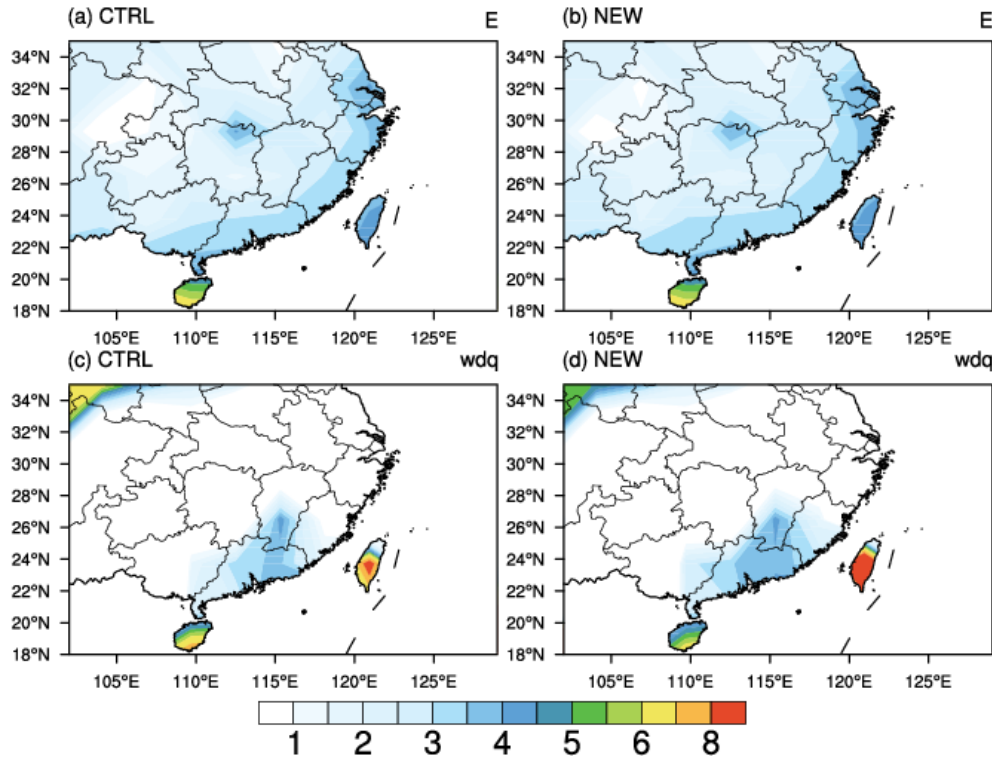
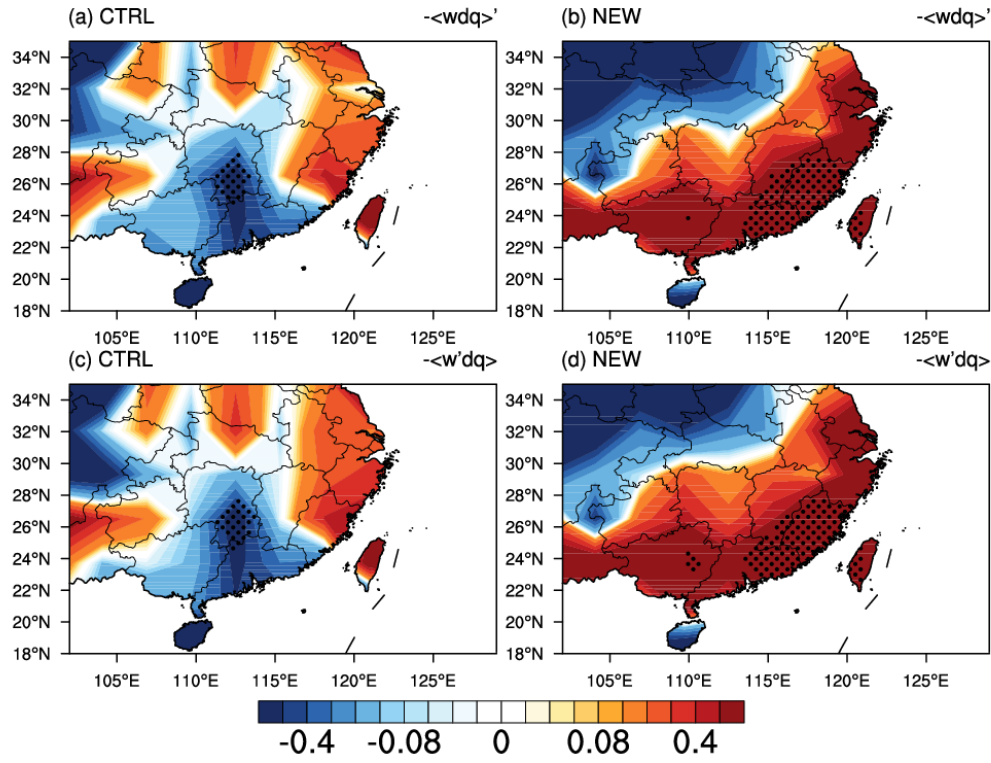


Figure 5. August mean evaporation (mm d^{-1}) for the (a) CTRL and (b) NEW simulations and vertical moisture advection (mm d^{-1}) for (c) CTRL and (d) NEW over the main rainfall regions during 1979–2008.

The linear trend (Figure 4b) in moisture-balance components indicates that the increasing trend in August rainfall over the main rainfall region, as described by the NEW simulation, is caused predominantly by enhanced vertical moisture advection (statistically significant at the 95% confidence level), whereas horizontal moisture advection and local evaporation make little contribution to the rainfall trend (Figure 4b). The difference in rainfall trends between the CTRL and NEW simulations is caused by the difference in vertical moisture advection. Vertical moisture advection was further decomposed into two components: the dynamic term, $-\langle w'dq \rangle$, and the thermodynamic component, $-\langle w dq' \rangle$, with the former predominating (Figure 4b). Spatial patterns of the linear trend in the dynamic term (Figure 6c, d) are consistent with those of vertical moisture advection (Figure 6a, b) and rainfall (Figure 2c, d). The differences in long-term trends for rainfall in the CTRL and NEW simulations

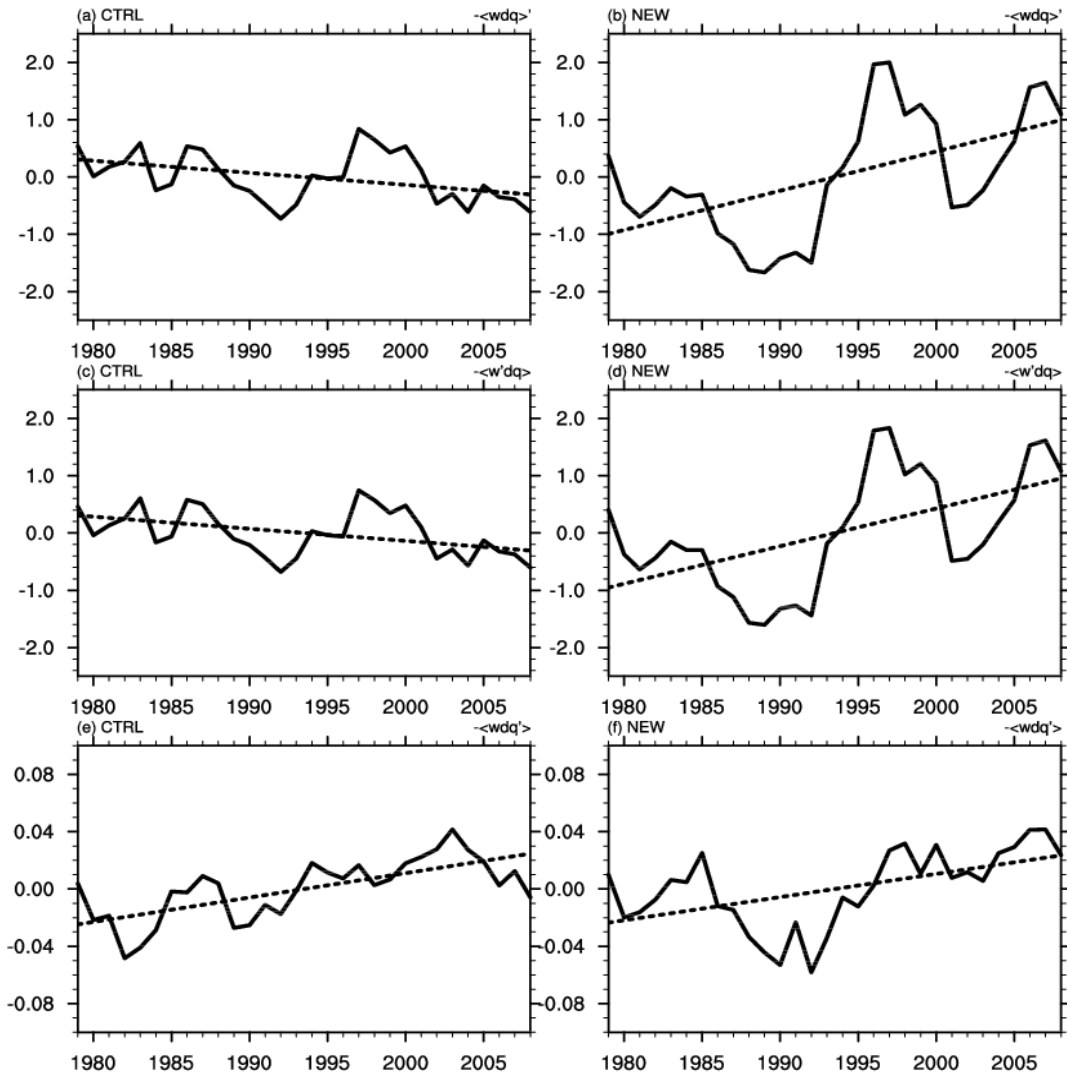
264 over the main rainfall regions are thus induced by dynamic component of vertical
265 moisture advection, relating with changing of atmospheric circulation.



267 **Figure 6.** Spatial distributions of the long-term trend in (a) vertical moisture
268 advection ($-\langle w dq \rangle'$) and (c) the dynamic component ($-\langle w' dq \rangle$) over the main
269 rainfall regions during 1979–2008 for CTRL and NEW (b, d) simulations, mm d⁻¹
270 decade⁻¹. Dotted areas indicate trends significant at the 90% confidence level.

271 Time series of vertical moisture advection anomalies and its thermodynamic and
272 dynamic components in the main rainfall regions are shown in Figure 7. The
273 anomalies exhibit negative and positive trends of -0.18 mm d⁻¹ decade⁻¹ and 0.68
274 mm d⁻¹ decade⁻¹ for 1979–2008 for the CTRL (Figure 7a) and NEW (Figure 7b)
275 simulations, respectively (statistically significant at the 95% confidence level).
276 Regarding long-term trends in the dynamic and thermodynamic components, the
277 former has significantly decreasing and increasing trends of -0.18 mm d⁻¹ decade⁻¹
278 and 0.64 mm d⁻¹ decade⁻¹ for the CTRL and NEW simulations (Figure 7c, d),
279 respectively, with almost the same magnitude as that of vertical moisture advection,

280 whereas the latter displays a weakly increasing trend of $0.02 \text{ mm d}^{-1} \text{ decade}^{-1}$ for both
 281 the CTRL and NEW simulations (Figure 7e, f). Thus, the discrepancies between the
 282 two simulations of long-term rainfall are also caused by changes in dynamic
 283 component of vertical moisture advection.



285 **Figure 7.** Time series (1979–2008) of (a) vertical moisture advection anomalies ($-\langle w dq \rangle'$), (c) the dynamic ($-\langle w' dq \rangle'$), and (e) thermal ($-\langle w dq \rangle$) components
 286 averaged over the main rainfall regions (mm d^{-1}) for the CTRL simulation; with (b, d,
 287 f) being likewise for the NEW simulation.

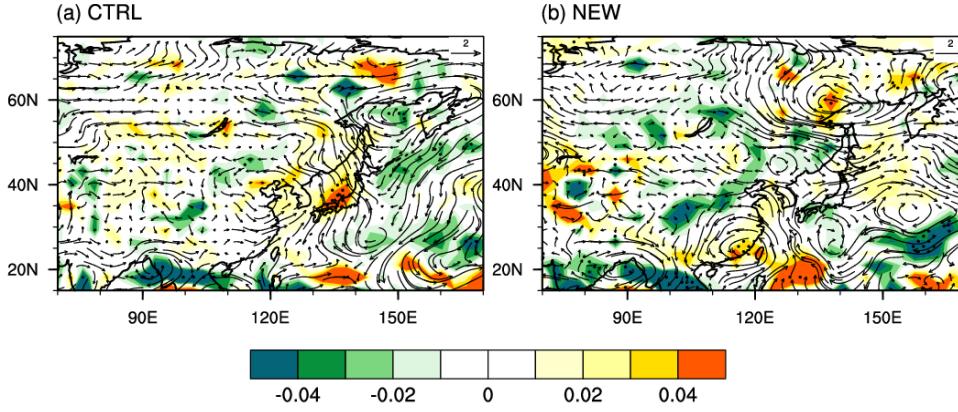


Figure 8. Spatial distributions of the linear trend for vertical velocity at 500hPa (ω_{500} shaded area, $-\text{Pa s}^{-1} 30\text{-yr}^{-1}$) and their associated large-scale circulation, as indicated by the 850hPa wind (vectors, $\text{m s}^{-1} 30\text{-yr}^{-1}$). (a) and (b) indicates the CTRL and NEW simulations, separately. The dotted areas are statistically significant at the $\geq 90\%$ confidence level.

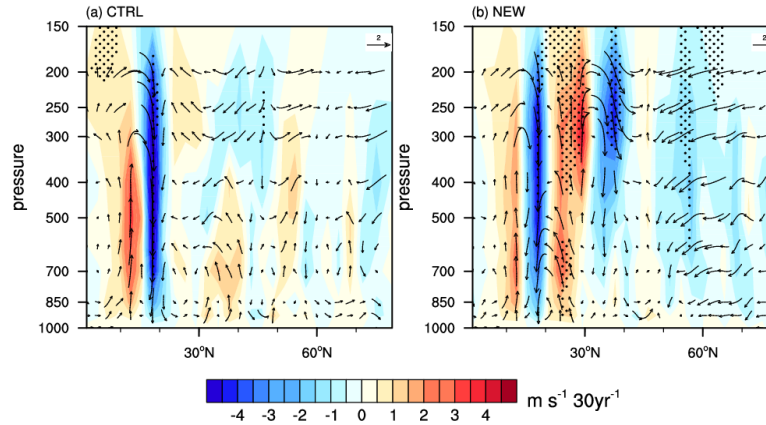


Figure 9. Zonal height cross-section of vertical velocity trends (shaded, ω , $\text{Pa s}^{-1} 30 \text{ yr}^{-1}$) and the trend in vertical velocity and meridional winds (vectors) at 90° – 125° E during 1979–2008 for the CTRL (a) and NEW (b) simulations. Dotted areas indicate the trend of vertical velocity at the 90% confidence level.

Based on the continuity equation

$$\nabla_h \cdot \vec{V}_h + \partial_p \omega = 0 \quad (6)$$

Which the first term in the left of the equation (6) indicates the horizontal convergence, and ω is the vertical velocity at the pressure coordination. If ω is zero at the surface, then its value at 500hPa (ω_{500}) approximates the convergence between the middle and lower troposphere. Spatial distributions of the linear trend in ω_{500} and

associated large-scale circulation at 850hPa are shown in Figure 8. Compared with the CTRL simulation, the NEW simulation indicates a significantly increasing trend in ω_{500} in the main rainfall region, accompanied by obvious convergence in the lower atmosphere (Figure 8b). In addition, there is a significantly strengthened ascending motion over 20°–30°N from the surface to the upper troposphere (Figure 9b), which is consistent with the area of increasing precipitation (Figure 2d) and with a northerly anomaly, especially in the upper-middle troposphere (Figure 9b). Correspondingly, wind at 850hPa exhibits a northerly anomaly in northern China, whereas the CTRL simulation indicates a southerly wind anomaly, implying that monsoon circulation weakened in the NEW simulation.

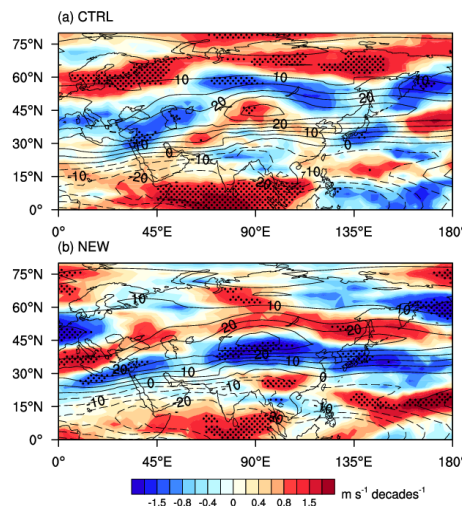


Figure 10. Linear (contours) and climatological (solid lines, westerly; dashed lines, easterly) trends in zonal wind at 200 hPa in August during 1979–2008. Dots represent significance of the trend in 200 hPa zonal wind at the 90% confidence level

Linear trend and climatological in 200hPa zonal winds in August during 1979–2008, as described by the two simulations, are shown in Figure 10. Both two tests simulate similar centers of climatological zonal wind at 200hPa at 45°N, although westerly winds at 200hPa exhibit respective weakening and strengthening trends in the NEW and CTRL simulations. Previous studies have found correlations between 200hPa

winds and summer precipitation in SC. For example, Kwon et al. (2007) reported that the mean June–August zonal wind speed at 200hPa has displayed a decreasing trend over East Asia since the mid-1990s, with a negative correlation with summer precipitation in southeastern China. Chen et al. (2014) reported that increased rainfall in SC around the mid-1990s coincided with decadal warming over northeastern Asia in association with a weakened subtropical westerly jet stream, which occurs only in summer (June, July, August). These findings are consistent with results of the NEW simulation.

3.3 Physical mechanisms

To further understand what causes the circulation changes between CTRL and NEW simulations, we compare the differences in two tests, and analyze how the differences affect the atmosphere circulation.

The CTRL and NEW simulations use different criteria for estimating soil freezing or melting (Table 1). At soil temperatures below 0°C, all liquid water in the soil layer would freeze gradually in the CTRL simulation, whereas the NEW simulation considers the effect of supercooled water with liquid water and ice coexisting over a wide range of temperatures below 0°C. This leads to differences in soil ice content between the two simulations, which reflect the decreasing of frozen soil at the background of global warming to a certain extent. Soil freeze–thaw processes are generally accompanied by phase transitions of soil water and result in the respective release and absorption of latent heat (Yang et al., 2007). Differences in soil ice content thus lead to soil temperature disparities between the two simulations.

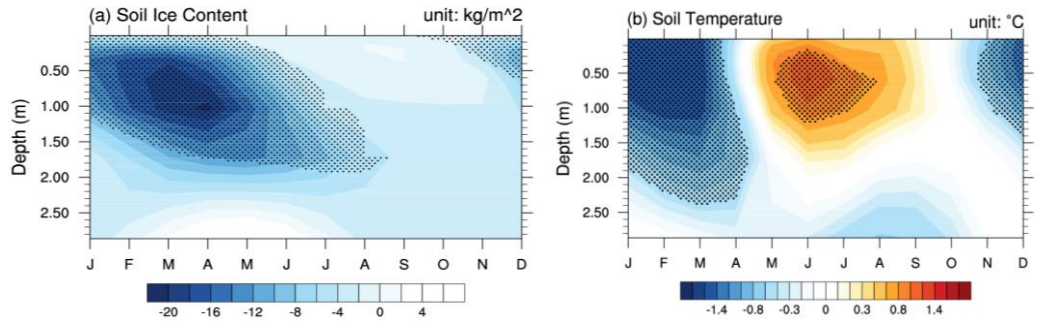


Figure 11. Time (month)–depth plots of differences in (a) soil water content (kg m^{-2}) and (b) soil temperature ($^{\circ}\text{C}$) between NEW and CTRL simulations at mid–high latitudes in Eurasia (45° – 60°N , 0° – 180°E). The dotted areas indicate differences significant at the 95% confidence level.

Typical frozen-soil regions of Eurasia at mid–high latitudes (45° – 60°N , 0° – 180°E) were considered here in examining the local impacts of the two simulations. The figure 11 shows the seasonal variations in the differences of soil ice content (kg m^{-2}) and soil temperature ($^{\circ}\text{C}$) between NEW and CTRL simulation in each soil layers over the Eurasia during 1979–2008. As air temperatures fall in autumn, soil temperature drops gradually to below 0°C and liquid water freezes from surface to the deeper soil layer. There is a negative difference of soil ice content between two simulations near the surface on October and the large negative differences appear in the deeper soil layer of 1 meter on March–April, because the soil temperature in the deeper soil layer has time-lag compared with that in the shallower soil layer. Meanwhile, CLM3.0 discretizes the soil column into 10 layers based on an exponential function, with the thickness of layers decreasing as depth increases; i.e., layers are thinner near the surface. Differences in simulated soil ice contents therefore increase with depth (Figure 11a).

A significantly negative soil temperature difference appears after November and spreads to deeper layers, reaching the 2.3 meter level in April, before a positive difference develops and reaches a maximum in June–July. The soil temperature

difference between the two simulations arises mainly because of the latent heat release or absorption during the respective freezing or melting processes. During autumn and winter, soil liquid water freezes and releases the latent heat of condensation, restraining the soil temperature decrease. The CTRL simulation thus provides a higher soil temperature than the NEW simulation in the cold season, when the soil ice content is higher. However, in the CTRL simulation, a higher soil ice content during the cold season would consume more energy during melting, resulting in less energy being absorbed by the soil, with the CTRL-simulated soil temperature therefore being slightly lower during May–August than that of the NEW simulation. Ice has a high thermal conductivity; therefore, during cold seasons the difference in soil temperature could spread further into the soil than the ice content (Figure 11b).

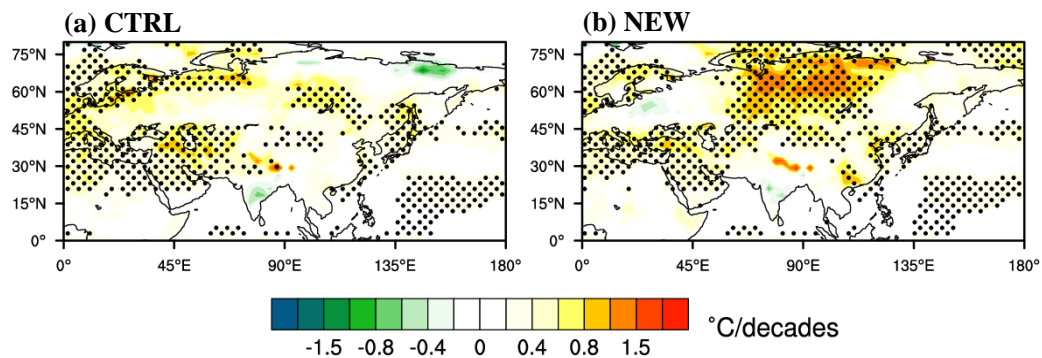


Figure 12. Spatial distributions of the linear trend for 2 m air temperature (shaded areas, $^{\circ}\text{C decade}^{-1}$) in August for the (a) CTRL and (b) NEW simulations during 1979–2008. The dotted areas are statistically significant at the 90% confidence level.

The response of the atmosphere to the soil thermal state was compared between the two simulations. Spatial distributions of the linear trend for 2 m air temperatures in August are shown in Figure 12, with both two simulations indicating spatially non-uniform warming trends. The NEW simulation indicates a warming trend north of 40°N relative to that of the CTRL simulation, especially in western–central Siberia (Figure 12), weakening the meridional thermal contrast and leading to a decrease in

the 200hPa westerly jet stream according to the thermal wind balance. This is consistent with the results shown in Figure 10.

To summarize, compared with the CTRL simulation, the NEW simulation have relatively little soil ice during autumn and winter due to the existence of supercooled water at temperatures below 0°C in seasonal frozen-soil regions. Because the phase change between water and ice is accompanied by the release and absorption of energy, the NEW simulation indicates a higher warming trend in 2 m air temperature in August, especially in western–central Siberia, producing a north–south temperature gradient opposing the original gradient produced by solar forcing and weakening the meridional thermal contrast. Based on thermal wind equations for a pressure surface, the 200hPa zonal winds weakened in the NEW simulation, with the blocking effect of the jet stream being reduced and the interaction between low- and high-latitude atmospheres strengthened (Zhu et al., 2011), and at 850hPa there is a northerly anomaly in northern China in August, with a weakening of the East Asian summer monsoon. Zhu et al. (2012) reported that this weakening is due mainly to the increasing surface air temperature over the Baikal region (45°–65°N, 80°–130°E) induced by greenhouse gases. The suppression of northerly winds to the south of China leads to convergence in the lower atmosphere and increasing vertical velocity in southeastern China, with precipitation increasing in that region in the NEW simulation.

4 Discussions and Conclusions

This study investigated the effects of soil freeze–thaw processes on August rainfall in SC by applying the GAMIL2.0 model with two different soil freeze–thaw schemes (the CTRL and NEW simulations) under the same climatological SST forcing.

414 Moisture-budget analysis was applied to elucidate rainfall differences between the
415 two simulations.

416 The intrinsic difference between two soil freeze–thaw schemes was the diversity of
417 the simulated soil ice content in soil layers, reflecting the response of frozen soil to
418 the global warming to some extent. The NEW simulation demonstrated that inclusion
419 of supercooled water in the soil freeze–thaw scheme reproduced the climatology and
420 trends of August precipitation in SC, indicating that the variability of soil freeze–thaw
421 processes influences August precipitation in SC. Furthermore, results indicate that the
422 climatological August rainfall in SC is largely attributable to evaporation, and
423 indicates the importance of land–atmosphere interaction over this region. The
424 dynamic component of vertical moisture advection ($-\langle w'dq \rangle$), which is related to
425 atmospheric circulation changes, has a significant influence on the August
426 precipitation trend, with the differences of simulated rainfall between two simulations
427 also being associated with $-\langle w'dq \rangle$.

428 The physical mechanisms were further explored to provide a simply explanations for
429 how the changing freeze–thaw processes during autumn and winter affect the August
430 rainfall in SC. The NEW simulation modeled the higher soil/air temperatures in
431 August especially in the north of 40°N, for simulating lower soil ice contents during
432 cold seasons, lead to the meridional thermal contrast weakened, and result in the
433 200hPa zonal winds decreased, indicating the blocking effect of the jet stream
434 reduced and the interaction between low- and high-latitude atmospheres strengthened,
435 therefore the northerly wind at 850hpa strengthened and was suppressed to the south
436 of China, which is more beneficial to the convergence of the lower atmosphere, and
437 thus causing vertical velocity increased and more precipitation. However, the
438 changing of freeze–thaw processes likely induced a Rossby wave-like pattern, thus

439 affecting August rainfall in SC. Previous studies have shown that the extension of
440 stationary Rossby waves in the upper troposphere at mid–high latitudes from Europe
441 to East China leads to a negative teleconnection between rainfall in SC and the East
442 Europe Plain in July and August (Su & Lu, 2014). The Eurasian spring snow anomaly
443 is associated with East Asian summer precipitation through the triggering of an
444 anomalous mid-latitude Eurasian wave train propagating eastward (Zhang et al.,
445 2017). Further analysis of the mechanism related to the wave-train propagating is
446 beyond the scope of this study.

447 To conclude, this study provides a new interpretation for the ‘southern flooding’
448 during 1979–2008 from the view of the changing in frozen soil, meanwhile, attention
449 should be paid to the frozen soil variability in the mid-high latitude at the background
450 of global warming, for their significant impact on the precipitation in SC regions, and
451 take effective measures to slow down the effect of the frozen soil changing.

452 453 454 Acknowledgements:

455 This work was supported by the National Key R&D Program of China (Grant No.
456 2017YFA0603902) and the National Science Foundation for Young Scientists of
457 China (Grant No. 41505080). The dataset of simulations by GAMIL2.0 were acquired
458 from the website of (<http://data.lasg.ac.cn/xiakun/>).

References

- Adler, R. F., Huffman, G. J., Chang, A., Ferraro, R., Xie., P., Janowiak, J., et al. (2003). The version-2 global precipitation climatology project (GPCP) monthly precipitation analysis (1979–present). *Journal of Hydrometeorology*, 4, 1147–1167. [https://doi.org/10.1175/1525-7541\(2003\)004<1147:tvgpscp>2.0.co;2](https://doi.org/10.1175/1525-7541(2003)004<1147:tvgpscp>2.0.co;2)
- Akinsanola, A.A., & Zhou, W. (2019). Dynamic and thermodynamic factors controlling increasing summer monsoon rainfall over the West African Sahel. *Climate Dynamics*, 52, 4501–4514. <https://doi.org/10.1007/s00382-018-4394-x>
- Chan J. C. L., & W. Zhou. (2005). PDO, ENSO and the early summer monsoon rainfall over South China. *Geophysical Research Letters*, 32, L08810. <https://doi.org/10.1029/2004GL022015>
- Chen, L., & Wu, R. (2000). Interannual and decadal variations of snow cover over Qinghai-Xizang Plateau and their relationships to summer monsoon rainfall in China. *Advances in Atmospheric Sciences*, 17, 18–30. <https://doi.org/10.1007/s00376-000-0040-7>
- Chen, Y., & Zhai, P. (2013). Persistent extreme precipitation events in China during 1951–2010. *Climate Research*, 57, 143–155. <https://doi.org/10.3354/cr01171>
- Chou, C., & Lan, C. (2012). Changes in the Annual Range of Precipitation under Global Warming. *Journal of Climate*, 25, 222–235. <https://doi.org/10.1175/JCLI-D-11-00097.1>
- Cox, P. M., Betts, R., Bunton, C., Essery, R., Rowntree, P., & Smith, J. (1999). The impact of a new land surface physics on the GCM simulation of climate and climate sensitivity. *Climate Dynamics*, 15(3), 183–203. <https://doi.org/10.1007/s003820050276>
- Frauenfeld, O. W., & Zhang, T. (2011). An observational 71-year history of seasonally frozen ground changes in the Eurasian high latitudes. *Environment Research Letters*, 6, 044024. <https://doi.org/10.1088/17489326/6/4/044024>
- Frauenfeld, O. W., Zhang, T., & McCreight, J. (2007). Northern hemisphere freezing/thawing index variations over the twentieth century. *International Journal of Climatology*, 27(1), 47–63. <https://doi.org/10.1002/joc.1372>

- 488 Ren, F., Gleason, B. & Easterling, D. (2002). Typhoon impacts on china's precipitation during
489 1957-1996. *Advances in Atmospheric Sciences*, 19, 943–952. [https://doi.org/10.1007/s00376-002-](https://doi.org/10.1007/s00376-002-0057-1)
490 0057-1
- 491 Ju, J., Lü, J., Cao, J., & Ren, J. (2005). Possible impacts of the Arctic Oscillation on the
492 interdecadal variation of summer monsoon rainfall in East Asia. *Advances in Atmospheric*
493 *Sciences*, 22, 39–48. <https://doi.org/10.1007/BF02930868>
- 494 Kwon, M. H., Jhun, J. G., & Ha, K. J. (2007). Decadal change in East Asian summer monsoon
495 circulation in the mid-1990s. *Geophysical Research Letters*, 34, L21706,
496 <https://doi.org/10.1029/2007GL031977>
- 497 Li, H., Dai, A., Zhou, T., & Lu, J. (2010). Responses of East Asian summer monsoon to historical
498 SST and atmospheric forcing during 1950–2000. *Climate Dynamics*, 34, 501–514.
499 <https://doi.org/10.1007/s00382-008-0482-7>
- 500 Li, L., Wang, B., Dong, L., Liu, L., Shen, S., Hu, N., et al. (2013). Evaluation of Grid-point
501 Atmospheric Model of IAP LASG Version 2 (GAMIL2). *Advances in Atmospheric Sciences*,
502 30(3), 855-867. <https://doi.org/10.1007/s00376-013-2157-5>
- 503 Li, P., Zhou, T. & Chen, X. (2018). Water vapor transport for spring persistent rains over
504 southeastern China based on five reanalysis datasets. *Climate Dynamics*, 51, 4243–4257.
505 <https://doi.org/10.1007/s00382-017-3680-3>
- 506 Li, W., Ren, H., Zuo, J., & Ren, H. (2018). Early summer southern China rainfall variability and
507 its oceanic drivers. *Climate Dynamics*, 50, 4691-4705. <https://doi.org/10.1007/s00382-017-3898-0>
- 508 Li, Y., & Leung, L. R. (2013) Potential impacts of the Arctic on interannual and interdecadal
509 summer precipitation over China. *Journal of Climate*, 26, 899–917. [https://doi.org/10.1175/JCLI-](https://doi.org/10.1175/JCLI-D-12-00075.1)
510 D-12-00075.1
- 511 Liu, J., Ren, H., Li, W., & Zuo, J. (2019). Diagnosing the leading mode of interdecadal
512 covariability between the Indian Ocean sea surface temperature and summer precipitation in
513 southern China. *Theoretical Applied Climatology*, 135, 1295–1306.
514 <https://doi.org/10.1007/s00704-018-2430-8>

- 515 Ma, H., Jiang, Z., Song, J., Yang, X., & Huo, F. (2015). Effects of urban land use change in East
516 China on the East Asian summer monsoon based on the CAM5.1 model. *Climate Dynamics*, 46,
517 2977-2989. <https://doi.org/10.1007/s00382-015-2745-4>
- 518 Menon, S., Hansen, J., Nazarenko, L., & Luo, Y. (2002). Climate effects of black carbon aerosols
519 in China and India. *Science*, 297, 2250-2253. <https://doi.org/10.1126/science.1075159>
- 520 Niu, G., & Yang, Z. (2006). Effects of frozen soil on snowmelt runoff and soil water storage at a
521 continental scale. *Journal of Hydrometeorology*, 7, 937-952. <https://doi.org/10.1175/JHM538.1>
- 522 Peng, X., Zhang, T., Frauenfeld, O. W., Wang, K., Cao, B., Zhong, X., et al. (2017). Response of
523 seasonal soil freeze depth to climate change across China. *Cryosphere*, 11, 1059–1073.
524 <https://doi.org/10.5194/tc-11-1059-2017>
- 525 Poutou, E., Krinner, G., Genthon, C., & de Noblet-Ducoudre, N. (2004) Role of soil freezing in
526 future boreal climate change. *Climate Dynamics*, 23, 621–639. [https://doi.org/10.1007/s00382-](https://doi.org/10.1007/s00382-004-0459-0)
527 004-0459-0
- 528 You, Q., Wu, T., Shen, L., Pepin, N., Zhang, L., Jiang, Z., et al. (2020). Review of snow cover
529 variation over the Tibetan Plateau and its influence on the broad climate system. *Earth-Science*
530 *Reviews*, 201, 103043. <https://doi.org/10.1016/j.earscirev.2019.103043>
- 531 Ren, F., Wu, G., Dong, W., Wang, X., Wang, Y., Ai, W., et al. (2006). Changes in tropical
532 cyclone precipitation over China. *Geophysical Research Letter*, 33, L20702.
533 <https://doi.org/10.1029/2006GL027951>
- 534 Schlosser, C., Slater, A., Robock, A., Pitman, A., Vinnikov, K., Henderson-Sellers, A., et al.
535 (2000) Simulations of a boreal grassland hydrology at Valdai, Russia: PILPS phase 2(d). *Monthly*
536 *Weather Review*, 128, 301-321. [http://dx.doi.org/10.1175/1520-](http://dx.doi.org/10.1175/1520-0493(2000)128<0301:soabgh>2.0.co;2)
537 0493(2000)128<0301:soabgh>2.0.co;2
- 538 Seager, R., Naik, N., & Vecchi, G. (2010). Thermodynamic and Dynamic Mechanisms for Large-
539 Scale Changes in the Hydrological Cycle in Response to Global Warming. *Journal of Climate*, 23,
540 4651–4668. <https://doi.org/10.1175/2010JCLI3655.1>
- 541 Shi, J., Cui, L., & Tian, Z. (2020). Spatial and temporal distribution and trend in flood and drought
542 disasters in East China. *Environmental Research*, 185, 109406.
543 <https://doi.org/10.1016/j.envres.2020.109406>

- 544 Si, D., & Ding, Y. (2013). Decadal change in the correlation pattern between the Tibetan Plateau
 545 winter snow and the East Asian summer precipitation during 1979–2011. *Journal of Climate*, 26,
 546 7622–7634. <https://doi.org/10.1175/JCLI-D-12-00587.1>
- 547 Si, D., & Ding, Y. (2016). Oceanic Forcings of the Interdecadal Variability in East Asian Summer
 548 Rainfall. *Journal of Climate*, 29, 7633–7649. <https://doi.org/10.1175/JCLI-D-15-0792.1>.
- 549 Su, Q., Lu, R. (2014). Teleconnection between rainfall over South China and the East European
 550 Plain in July and August. *Theoretical and Applied Climatology*, 118, 185-194.
 551 <https://doi.org/10.1007/s00704-013-1058-y>
- 552 Su, Q., Lu, R., & Li, C. (2014). Large-scale Circulation Anomalies Associated with Interannual
 553 Variation in Monthly Rainfall over South China from May to August. *Advances in Atmospheric*
 554 *Sciences*, 31(2), 273-282. <https://doi.org/10.1007/s00376-013-3051-x>
- 555 Sun, J., & Wang, H. (2012) Changes of the connection between the summer North Atlantic
 556 Oscillation and the East Asian summer rainfall. *Journal of Geophysical Research*, 117, D08110,
 557 <https://doi.org/10.1029/2012JD017482>
- 558 Viterbo, P., Beljaars, A., Mahfouf, J., & Teixeira, J. (1999). The representation of soil moisture
 559 freezing and its impact on the stable boundary layer. *Quarterly Journal of the Royal*
 560 *Meteorological Society*, 125, 2401-2426. <https://doi.org/10.1002/qj.49712555904>
- 561 Wang, B., Liu, J., Yang, J., Zhou, T., Wu, Z. (2009). Distinct principal modes of early and late
 562 summer rainfall anomalies in East Asia. *Journal of Climate*, 22, 3864-3875.
 563 <https://doi.org/10.1175/2009JCLI2850.1>
- 564 Wang, B., & Ji, Z. (2006). New numerical methods and their applications in the atmospheric
 565 science. *Science Press*, 208pp.
- 566 Wang, B., Wan, H., Ji, Z., Zhang, X., Yu, R., Yu, Y., et al. (2004). Design of a new dynamical
 567 core for global atmospheric models based on some efficient numerical methods. *Science in China*
 568 *(Math)*, 47, 4-21.
- 569 Wu, B., Yang, K. & Zhang, R. (2009). Eurasian snow cover variability and its association with
 570 summer rainfall in China. *Advances in Atmospheric Sciences*, 26, 31–44.
 571 <https://doi.org/10.1007/s00376-009-0031-2>

- 572 Wu, R., Wen, Z., Yang, S. & Li, Y. (2010). An Interdecadal Change in Southern China Summer
573 Rainfall around 1992/93. *Journal of Climate*, 23, 2389–2403,
574 <https://doi.org/10.1175/2009JCLI3336.1>
- 575 Wu, T., & Qian, Z. (2003). The relation between the Tibetan winter snow and the Asian summer
576 monsoon and rainfall: An observational investigation. *Journal of Climate*, 16, 2038–2051.
577 [https://doi.org/10.1175/1520-0442\(2003\)016<2038:TRBTTW>2.0.CO;2](https://doi.org/10.1175/1520-0442(2003)016<2038:TRBTTW>2.0.CO;2)
- 578 Wu, X., & Mao, J. (2017). Interdecadal variability of early summer monsoon rainfall over South
579 China in association with the Pacific Decadal Oscillation. *International Journal of Climatology*,
580 37, 706–721. <https://doi.org/10.1002/joc.4734>
- 581 Xie, P., & Arkin, P. (1997). Global precipitation: A 17-year monthly analysis based on gauge
582 observations, satellite estimates, and numerical model outputs. *Bulletin of the American*
583 *Meteorological Society*, 78, 2539 – 2558. [https://doi.org/10.1175/1520-](https://doi.org/10.1175/1520-0477(1997)078<2539:GPAYMA>2.0.CO;2)
584 [0477\(1997\)078<2539:GPAYMA>2.0.CO;2](https://doi.org/10.1175/1520-0477(1997)078<2539:GPAYMA>2.0.CO;2)
- 585 Xin, Y., Wu, B., Bian, L., Liu, G., Zhang, L., Li, R., et al. (2012). The response of the East Asia
586 climate system to the water and heat change of the global frozen soil using NCAR CAM model.
587 *Chinese Science Bulletin*, 57, 2872–2881. <https://doi.org/10.1007/s11434-012-5361-2>
- 588 Yang, M., Yao, T., Gou, X., Hirose, N., Fujii H., Hao, L., et al. (2007). Diurnal freeze/thaw cycles
589 of the ground surface on the Tibetan Plateau. *Chinese Science Bulletin*, 52, 136–139.
590 <https://doi.org/10.1007/s11434-007-0004-8>
- 591 Yuan, C., Liu, J., Luo, J., Guan, Z. (2019). Influences of Tropical Indian and Pacific Oceans on
592 the Interannual Variations of Precipitation in the Early and Late Rainy Seasons in South China.
593 *Journal of Climate*, 32, 3681–3694. <https://doi.org/10.1175/JCLI-D-18-0588.1>
- 594 Zhang, R., Wu, B., Han, J., & Zuo, Z. (2013). Effects on summer monsoon and rainfall change
595 over China due to Eurasian snow cover and ocean thermal conditions. *Climate Change: Realities,*
596 *Impacts over Ice Cap, Sea Level and Risks*, B. R. Singh, Ed., InTech, 227–250
- 597 Zhang, Y., & Li, D. (2019). Drought-flood abrupt alternation and its atmospheric circulation
598 characteristics during flood season in southern China. *Climatic and Environmental Research (in*
599 *Chinese)*, 24(4), 430–444. <https://doi.org/10.3878/j.issn.1006-9585.2018.18024>

600 Zhang, R., Zhang, R., & Zuo, Z. (2017). Impact of Eurasian Spring Snow Decrement on East
601 Asian Summer Precipitation. *Journal of Climate*, 30(9), 3421-3437. [https://doi.org/10.1175/JCLI-](https://doi.org/10.1175/JCLI-D-16-0214.1)
602 D-16-0214.1

603 Zhu, C., Wang, B., Qian, W., & Zhang, B. (2012). Recent weakening of northern East Asian
604 summer monsoon: A possible response to global warming. *Geophysical Research Letters*, 39,
605 L09701. <https://doi.org/10.1029/2012GL051155>

606 Zhu, Y., Wang, H., Ma, J., Wang, T., & Sun, J. (2015). Contribution of the phase transition of
607 Pacific Decadal Oscillation to the late 1990s' shift in East China summer rainfall. *Journal of*
608 *Geophysical Research: Atmospheres*, 120, 8817-8827. <https://doi.org/10.1002/2015JD023545>

609 Zhu, Y., Wang, H., Zhou, W., & Ma, J. (2011). Recent changes in the summer precipitation
610 pattern in East China and the background circulation. *Climate Dynamics*, 36, 1463–1473.
611 <https://doi.org/10.1007/s00382-010-0852-9>
612
613